

Sign problem free quantum Monte-Carlo study on thermodynamic properties and magnetic phase transitions in orbital-active itinerant ferromagnets

Shenglong Xu,¹ Yi Li,² and Congjun Wu¹

¹*Department of Physics, University of California, San Diego, California 92093, USA*

²*Princeton Center for Theoretical Science, Princeton University, Princeton, New Jersey 08544, USA*

The microscopic mechanism of itinerant ferromagnetism is a long-standing problem due to the lack of non-perturbative methods to handle strong magnetic fluctuations of itinerant electrons. We have non-perturbatively studied thermodynamic properties and magnetic phase transitions of a two-dimensional multi-orbital Hubbard model exhibiting ferromagnetic ground states. Quantum Monte-Carlo simulations are employed, which are proved in a wide density region free of the sign problem usually suffered by simulations for fermions. Both Hund's coupling and electron itinerancy are essential for establishing the ferromagnetic coherence. No local magnetic moments exist in the system *a priori*, nevertheless, the spin channel remains incoherent showing the Curie-Weiss type spin magnetic susceptibility down to very low temperatures at which the charge channel is already coherent exhibiting a weakly temperature-dependent compressibility. For the SU(2) invariant systems, the spin susceptibility further grows exponentially as approaching zero temperature in two dimensions. In the paramagnetic phase close to the Curie temperature, the momentum space Fermi distributions exhibit strong resemblance to those in the fully polarized state. The long-range ferromagnetic ordering appears when the symmetry is reduced to the Ising class, and the Curie temperature is accurately determined. These simulations provide helpful guidance to searching for novel ferromagnetic materials in both strongly correlated *d*-orbital transition metal oxide layers and the *p*-orbital ultra-cold atom optical lattice systems.

PACS numbers: Subject area: magnetism, condensed matter physics, atomic molecular and optical physics

I. INTRODUCTION

Itinerant ferromagnetism (FM) is one of the central topics of condensed matter physics [1–23]. It has also become a research focus both experimental and theoretical of ultra-cold atom physics [24–31]. The mechanism of itinerant FM has been a long-standing problem. Stoner proposed the exchange interaction among electrons with parallel spins as the driving force for itinerant FM [1]. Along this direction, the local density approximation (LDA) of the density functional theory has achieved great success [32, 33]. For example, the ground state magnetic moments of FM metals can be calculated accurately [34]. The implementation of correlation effects in LDA has also been improved by the methods of LDA+U [35], LDA+DMFT (dynamical mean-field theory) [36–38], and LDA+GP (Gutzwiller projection) [39–41].

Nevertheless, itinerant FM systems are also strongly correlated, and their physics is often non-perturbative. Usually repulsive interactions need to be sufficiently strong to overcome the kinetic energy cost of polarizing electron spins, and thus itinerant FM has no well-controlled weak-coupling starting point. The Stoner criterion overlooks correlation effects among electrons with opposite spins [23]: Electrons can delicately organize their wavefunctions to reduce repulsions and still remain unpolarized even in the presence of strong interactions. For example, the Lieb-Mattis theorem proves that the ground state of a rigorously one-dimensional (1D) system is a spin singlet no matter how strong the interaction is [5].

It is more appropriate to start with electron orbitals to construct lattice model Hamiltonians to address the strong correlation aspect of itinerant FM. Exact theorems establishing FM, which are usually based on lattice models, are indispensable to provide reference points for further investigations. Well-known examples include the Nagaoka theorem [6, 42–46], which applies to the infinite *U* Hubbard models in two and above dimensions with doping a single hole on the half-filled background, and the “flat-band” FM in certain lattices with dispersionless band structures [13, 47]. In the former case, FM arises because the spin polarized background maximally facilitates the hole's coherent hopping, while in the latter case, the band flatness reduces the kinetic energy cost for polarizing spin to zero.

One central issue of itinerant FM is the role of orbital degeneracy which widely exists in FM metals. Hund's coupling is a prominent feature in multi-orbital systems, which favors electrons on the same site to align their spins. However, Hund's coupling is local physics which usually cannot polarize itinerant electrons in the absence of local moments. Under what precise conditions Hund's coupling can lead to the global FM coherence in itinerant systems is still an open question.

The difficulty in achieving unambiguous FM ground states is only one side of the story of strongly-correlated itinerant FM, the finite-temperature thermodynamic properties are another challenge [10, 48–50]. At first looking, it might not look so striking: the ferromagnetic susceptibilities show the standard mean-field Curie-Weiss

(CW) law in the off-critical region as

$$\chi(T) = \frac{C}{T - T_0}, \quad (1)$$

where C is the Curie constant [51] and T_0 is the Curie temperature at the mean-field level. The CW law manifests spin incoherence, which is common in the paramagnetic state based on local moments. But it is difficult to understand in itinerant FM metals still possessing Fermi surfaces. For example, the transport and the charge channel properties, such as resistance and compressibility, remain metallic, *i.e.*, they are featured by the Fermi surface physics.

Within the itinerant picture, the Pauli magnetic susceptibility augmented by the random phase approximation (RPA) yields $\chi(T) \propto 1/(T^2 - T_0^2)$, but it is not commonly observed in experiments [10, 49, 50]. In fact, the CW law in FM metals applies to a wide range of temperatures $T_f \gg T > T_0$ (T_f is the Fermi temperature) which shows spin-incoherence well below T_f . The reason is that RPA treats the paramagnetic phase as a weakly correlated Fermi liquid state with slightly thermally broadened Fermi distributions. Actually, this phase is rather complicated: Dynamic FM domains strongly fluctuate, which is beyond the RPA description and is difficult to handle analytically. The paramagnetic state of itinerant FM exhibits much higher entropy capacity than the usual weakly correlated paramagnetic Fermi liquid state, which significantly suppresses the genuine Curie temperature T_c , or, the renormalized one, away from the mean-field value T_0 . Consequently, T_c is often significantly overestimated by weak coupling approaches [10, 49, 50].

A key question is how itinerant systems can exhibit the CW law and further develop FM purely based on itinerant electrons without involving local moments such that the charge channel remains coherent? Significant efforts have been made, including the self-consistent renormalization theory including spin mode coupling [9, 10, 48], the direct exchange from the Coulomb integral [11, 52], spin incoherence due to Hund's coupling [53], and the orbital-selective Mott transition [54, 55]. An important progress is that the CW law can be obtained from the combined method of LDA+DMFT [56] away from the critical region. However, none of these methods are non-perturbative in nature.

Another issue is the nature of the FM phase transitions in FM metals, which has been widely studied but is still under intensive debates [8, 14, 16–19]. Compared to the superconducting phase transitions in which the fermion degree of freedom is gapped below transition temperatures, the FM phase transitions are more involved because systems remain gapless across transitions due to the existence of Fermi surfaces. The FM domain fluctuations combined with the Landau damping of particle-hole excitations around Fermi surfaces complicates FM transitions. It would be important to perform a non-perturbative study.

Recently, the ground states of a multi-orbital Hub-

bard model have been proved fully spin polarized in the strong coupling regime in the 2D square and 3D cubic lattices [21] by two of the authors and Lieb. It is showed that inter-orbital Hund's coupling combined with electron itinerancy in the quasi-1D band structure drive the FM ground states. Compared to the Nagaoka FM, this new theorem proves a stable FM phase with nodeless ground state wavefunctions over the entire electron density region $0 < n < 2$, where n is the occupation number per site, thus it sets up a solid starting point for further studying the strong correlation aspect of itinerant FM. It also opens up the possibility of performing sign-problem free quantum Monte Carlo (QMC) simulations away from half-filling by employing the bases under which the many-body Hamiltonians satisfy the Perron-Frobenius condition.

Although this theorem only sets up the ground state properties, it establishes an unambiguous FM phase as a starting point for further studying both thermodynamic properties and magnetic phase transitions over a wide region of electron density. In order to handle the strong magnetic fluctuations, QMC simulations would be the ideal method, however, they usually suffer the notorious sign problem for fermions and thus are generally speaking inapplicable for itinerant FM. Remarkably, we prove that for the systems in which the ground state FM theorem mentioned above [21] applies, the fermion sign problem can be eliminated in the entire electron density region. This provides a new opportunity to study the finite temperature thermodynamic properties and magnetic phase transitions in an asymptotically exact way.

For later convenience, we briefly discuss the FM critical fluctuations which are particularly important in two-dimensions. According to the Landau-Ginzburg-Wilson paradigm of critical phenomena, T_c is suppressed from T_0 but remains finite in 3D. As T is lowered from T_0 and approaches T_c , the system crosses over from the mean-field region to the critical region, and $\chi(T) \propto (T - T_c)^{-\gamma}$ due to non-Gaussian fluctuations and γ is the critical exponent. In 2D, T_c remains finite if the system symmetry is reduced to the Ising class, or, the easy axis class. However, for the isotropic class, thermal fluctuations suppress T_c to zero according to the Mermin-Wagner theorem [57, 70]. Nevertheless, even in this case the mean-field T_0 is still an important temperature scale below which the FM order develops its magnitude. However, the orientation fluctuations of the FM order suppress the long-range order. In other words, this region is characterized by fluctuating FM domains and the correlation length increases exponentially as lowering temperatures. Consequently, the FM susceptibility deviates from the CW law and crosses over into an exponential growth.

In this article, we will present a systematic non-perturbative study on thermodynamic properties and magnetic phase transitions of itinerant FM by performing the sign-problem free QMC simulations. Our results show that itinerant FM can indeed exhibit both spin incoherence and charge coherence simultaneously without

forming local moments. In other words, the system exhibits the feature of the CW metal as a combined effect of Hund's coupling and electron itinerancy. The model we simulate can be realized in both d -orbital transition metal oxide layer and p -orbital ultra-cold atom optical lattices, which do not contain local moments a priori. The spin magnetic susceptibility exhibits the CW law as a signature of spin incoherence, while, the compressibility weakly depends on temperature as a consequence of itinerancy. The mean-field Curie temperature T_0 is extracted based on the CW law in the off-critical region, which is much lower than the temperature scale of charge coherence T_{ch} . The filling dependence of T_0 is calculated and the maximal T_0 reaches one tenth of the hopping integral. The Fermi distribution functions in momentum space are calculated in the strongly correlated paramagnetic phase. The fermion occupation numbers are strongly suppressed from the saturated value even for wavevectors close to the center of the Brillouin zone. When entering the critical region, for the SU(2) symmetric models, $\chi(T)$ grows exponentially. The true FM long range order is achieved by reducing the model symmetry to the Ising class and the FM critical temperature T_c is determined accurately by the finite size and critical scaling.

The rest part of this article is organized as follows. In Sect. II, the model Hamiltonian is introduced, and the QMC method for this model is proved free of the sign problem. The QMC simulations on the thermodynamic properties in the off-critical region is presented in Sect. III, and the momentum space Fermi distributions are calculated in Sect. IV. The results in the critical region are presented in Sect. V. In Sect. VI, we discuss the physics when the conditions for the absence of the sign problem are loosed. In particular, the simulations in the presence of a small inter-chain hopping, in which the sign problem appears but is not severe, are presented. The experimental realizations are discussed in Sect. VII. Conclusions are made in Sect. VIII.

II. THE MODEL HAMILTONIAN AND THE ABSENCE OF THE SIGN PROBLEM

In this section, we present the model Hamiltonians, whose ground states were proved to be ferromagnetic [21]. Furthermore, we also explain that the QMC sign-problem is absent, and thus, this model provides an ideal preliminary to study the thermodynamic properties and magnetic phase transitions of strongly-correlated itinerant FM in a controllable way.

A. The model Hamiltonians

We consider the case of the 2D square lattice: On each site there are two orthogonal orbitals forming a quasi-1D band structure. For simplicity, below we use the 2D p -orbital system as an example, and the physics is also

valid for the d_{xz} and d_{yz} -orbitals systems in 2D. The relevance of this model to the current experiment efforts of searching for novel itinerant FM systems will be discussed in Sect. VI. For the band structure, we only keep the σ -bonding t_{\parallel} term, i.e., electrons in the $p_{x(y)}$ -orbital only move longitudinally along the $x(y)$ -direction, respectively. The following Hamiltonian is defined in the square lattice as

$$H_{kin,\parallel} = -t_{\parallel} \sum_{\vec{r},\sigma} \left\{ p_{x\sigma}^{\dagger}(\vec{r} + \hat{e}_x) p_{x\sigma}(\vec{r}) + p_{y\sigma}^{\dagger}(\vec{r} + \hat{e}_y) \right. \\ \left. \times p_{y\sigma}(\vec{r}) + h.c. \right\} - \mu \sum_{\vec{r}} n(\vec{r}), \quad (2)$$

in which we neglect the small transverse bonding t_{\perp} -term. For realistic p -orbital systems, the sign of t_{\parallel} is negative due to the odd parity of p -orbital Wannier wavefunctions. Nevertheless, for the bipartite lattice such as the square lattice, the sign of t_{\parallel} can be flipped by a gauge transformation. Without loss of generality, t_{\parallel} is scaled to 1 below, which serves as the unit for all other quantities carrying energy unit in this article.

The interaction part H_{int} contains the standard multi-orbital Hubbard interaction [58–61] as

$$H_{int} = U \sum_{\vec{r},a=x,y} n_{a,\uparrow}(\vec{r}) n_{a,\downarrow}(\vec{r}) + V \sum_{\vec{r}} n_x(\vec{r}) n_y(\vec{r}) \\ - J \sum_{\vec{r}} \left\{ \vec{S}_x(\vec{r}) \cdot \vec{S}_y(\vec{r}) - \frac{1}{4} n_x(\vec{r}) n_y(\vec{r}) \right\} \\ + \Delta \sum_{\vec{r}} \left\{ p_{x\uparrow}^{\dagger}(\vec{r}) p_{x\downarrow}^{\dagger}(\vec{r}) p_{y\downarrow}(\vec{r}) p_{y\uparrow}(\vec{r}) + h.c. \right\}, \quad (3)$$

where $a = x, y$ referring to the orbital index; $n_{a,\sigma} = p_{a,\sigma}^{\dagger} p_{a,\sigma}$ and $n_a = n_{a,\uparrow} + n_{a,\downarrow}$; $\vec{S}_a = p_{a,\alpha}^{\dagger} \vec{\sigma}_{\alpha\beta} p_{a,\beta}$ is the spin operator of the a -orbital. The U and V -terms describe the intra- and inter-orbital Hubbard interactions, respectively; the J -term is Hund's coupling and $J > 0$ represents its FM nature; the Δ -term describes the pairing hopping process between two orthogonal orbitals.

In order to gain an intuitive understanding of the interaction parameters, let us consider a single site problem. There are in total six states which can be classified as a set of spin triplet states and three different spin singlet states. The triplet states are with energy V , defined as

$$p_{x,\uparrow}^{\dagger} p_{y,\uparrow}^{\dagger} |0\rangle, \quad \frac{1}{\sqrt{2}} (p_{x,\uparrow}^{\dagger} p_{y,\downarrow}^{\dagger} + p_{x,\downarrow}^{\dagger} p_{y,\uparrow}^{\dagger}) |0\rangle, \quad p_{x,\downarrow}^{\dagger} p_{y,\downarrow}^{\dagger} |0\rangle, \quad (4)$$

respectively, where $|0\rangle$ is the vacuum state. The other three spin singlet states are

$$\frac{1}{\sqrt{2}} (p_{x,\uparrow}^{\dagger} p_{y,\downarrow}^{\dagger} - p_{x,\downarrow}^{\dagger} p_{y,\uparrow}^{\dagger}) |0\rangle, \quad p_{x,\uparrow}^{\dagger} p_{x,\downarrow}^{\dagger} |0\rangle, \quad p_{y,\uparrow}^{\dagger} p_{y,\downarrow}^{\dagger} |0\rangle, \quad (5)$$

among which the first one involves both orbitals and its energy is $V + J$; the other two singlets only occupy the same orbital with the average energy U and the hybridization matrix element between them is Δ . In the

limit of $U \rightarrow +\infty$, the states of $p_{x,\uparrow}^\dagger p_{x,\downarrow}^\dagger |0\rangle$, and $p_{y,\uparrow}^\dagger p_{y,\downarrow}^\dagger |0\rangle$ are projected out. Nevertheless, the other four doubly occupied states are kept in the physical Fock space, including one set of spin-triplet states and one inter-orbital singlet state.

The ground states of the Hamiltonians Eq. 2 plus Eq. 3 are fully spin polarized at any generic filling n for arbitrary values of V under the condition that $U \rightarrow +\infty$ and $J > 0$. The detailed proof and its generalization to the 3D cubic lattice are presented in Ref. [21]. Below we present an intuitive physical picture. The band structure of Eq. 2 is quasi-1D, consisting of orthogonal rows and columns, and electrons do not transit among different lines. In the absence of Hund's coupling, then the intra-chain physics in the limit of $U \rightarrow +\infty$ would correspond to the 1D infinite- U Hubbard model whose ground states are highly degenerate regardless of the spin configurations. Then let us turn on $J > 0$, and the inter-chain Hund's coupling lifts the degeneracy and selects the fully polarized state as the unique ground state: When one electron in a row meets another one in a column at the crossing site, their spins are aligned to save the energy of J . Thus different from the usual case that Hund's coupling can only polarize electrons on the same site. Remarkably, in this case it does polarize electrons in the entire system [20, 21]. Although the electron band structure is quasi-1D, interactions couple electron spins in different chains together, and thus, the FM correlations and ordering are genuinely 2D, or, 3D.

For completeness, we also present the Hamiltonian of the inter-chain hopping with a small value of t_\perp as

$$H_{kin,\perp} = -t_\perp \sum_{\vec{r},\sigma} \left\{ p_{x\sigma}^\dagger(\vec{r} + \hat{e}_y) p_{x\sigma}(\vec{r}) + p_{y\sigma}^\dagger(\vec{r} + \hat{e}_x) p_{y\sigma}(\vec{r}) + h.c. \right\}, \quad (6)$$

which will be used in Sect. VIA. Again, in the square lattice the sign of t_\perp can be flipped by a gauge transformation, and without loss of generality, it is assumed to be positive. We set $t_\perp = 0$ in most part of this article except in Sect. VIA.

B. The absence of the QMC sign problem

The many-body Hamiltonian matrix of Eq. 2 plus Eq. 3 possesses an important sign structure in the limit of $U \rightarrow +\infty$ under which the ground state FM theorem applies [21]. In the coordinate representation, a convenient set of many-body bases are defined by ordering fermions according to their real space positions along one row by another and then along one column by another. The periodical and anti-periodical boundary conditions are employed for each chain if the particle number in that chain is odd and even, respectively, which is feasible because the particle number in each chain is separately conserved. This particular choice of boundary conditions should not

change the bulk physics. Under these bases and boundary conditions, in the limit of $U \rightarrow +\infty$, the electron hopping term and the spin-flip term from Hund's coupling do not change the sequence of fermion ordering. When electrons hop across the boundary, no extra minus sign appears either due to the above boundary condition. Then the many-body Hamiltonian matrix satisfies the prerequisite of the Perron-Frobenius theorem: All the non-zero off-diagonal matrix elements are either $-t$ or $-J$ arising from the kinetic energy term and Hund's coupling, respectively, and thus they are semi-negative-definite. We do not need to consider the pair hopping process which is completely suppressed in the limit of $U \rightarrow +\infty$. Remarkably, the above sign structure of the off-diagonal matrix elements renders the ground state many-body wavefunction nodeless, and also leads to the disappearance of the QMC sign problem for the ground states.

For the finite temperature thermodynamic properties, we use the stochastic series expansion (SSE) QMC method with the directed loop update algorithm [62–66]. This method is usually used for boson systems and 1D fermion systems. In our case, although the band structure of Eq. 2 is quasi-1D like, the interaction Eq. 3 couples all the chains together. In particular, the total spin of each chain is not conserved, and thus its magnetic properties in truly 2D. Remarkably, we find for this model the sign problem is absent at finite temperatures in the entire electron density region $0 < n < 2$. In the SSE method, the partition function is expanded as

$$Z = \sum_{n=0}^{+\infty} \frac{\beta^n}{n!} \sum_{\alpha_i^n} \prod_{i=1}^n \langle \alpha_i^n | -H | \alpha_{i-1}^n \rangle, \quad (7)$$

where $H = H_{kin,\parallel} + H_{int}$; $|\alpha_i^n\rangle$ runs over the set of many-body bases defined above and $|\alpha_n^n\rangle = |\alpha_0^n\rangle$. A negative constant is added to the many-body Hamiltonian matrix to make all of its diagonal matrix elements negative, and then all the matrix elements of $-H$ become positive. The grand canonical ensemble is employed to ensure the ergodicity of the particle number distribution in each chain. The parameters for the QMC simulations are provided in Appendix A.

The QMC sign problem does appear in the presence of the t_\perp -term, i.e., Eq. 6, because electrons become mobile in a two-dimensional manner. Nevertheless, the QMC simulations can still be performed when the sign problem is not so severe, which will be presented in Sect. VIA.

III. THERMODYNAMIC QUANTITIES IN THE OFF-CRITICAL REGION

In this section, we present the results of QMC simulations on the spin magnetic susceptibility $\chi(T)$ and the compressibility $\kappa(T)$ in the off-critical temperature region. $\chi(T)$ exhibits the celebrated CW law at temperatures well-below the kinetic energy scale of the system,

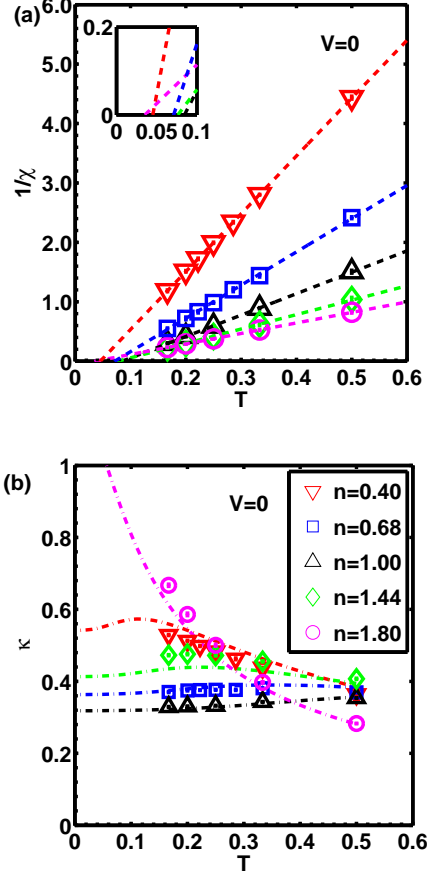


FIG. 1: (a) $\chi^{-1}(T)$ exhibits the CW law at different values of n . The inset shows interceptions corresponding to the mean-field value of Curie temperature T_0 . (b) The compressibility $\kappa(T)$ at different values of n . The dashed lines represent $\kappa(T)$ of 1D spinless fermions at the same densities for comparison. Values of n in (a) and (b) are represented by the same legend. $V = 0$ and $J = 2$ for both figures. The error bars of the QMC data are smaller than the symbols.

while $\kappa(T)$ typically weakly depends on temperature.

A. The temperature dependence of spin susceptibility $\chi(T)$ and compressibility $\kappa(T)$

The spin susceptibility χ and compressibility κ are two fundamental thermodynamic properties in interacting fermion systems in the spin and charge channels, respectively. In usual paramagnetic Fermi liquid states, both χ and κ at zero temperature exhibit the itinerant feature controlled by the density of states at the Fermi energy. Furthermore, they are renormalized by interaction effects characterized by the Landau parameters F_a^0 and F_s^0 in the spin and charge channels, respectively. At finite temperatures much lower than the Fermi temperature, $\chi(T)$ and $\kappa(T)$ are only weakly temperature dependent. However, in FM metals $\chi(T)$ and $\kappa(T)$ behave

dramatically differently exhibiting local-moment-like and itinerant features, respectively, which will be shown from the QMC simulation results.

Because the total spin is conserved, the spin magnetic susceptibility χ is represented by the equal-time correlation function as

$$\chi(T) = \lim_{L \rightarrow +\infty} \frac{\beta}{L^2} \sum_{\vec{r}_1, \vec{r}_2} \langle S_z(\vec{r}_1) S_z(\vec{r}_2) \rangle. \quad (8)$$

The QMC results of $\chi^{-1}(T)$ at $V = 0$ are presented in Fig. 1 (a) in the off-critical region based on the finite size scalings shown in Appendix B. For all the values of n presented, χ exhibits the CW-law in the off-critical region. The values of T_0 extracted from the linear form $\chi^{-1}(T)$ range from 0.01 to 0.1, which means that spin remains incoherent at temperatures well below t_{\parallel} (scaled to 1).

It is not surprising that $\chi(T)$ should asymptotically scale as $1/T$ in the high temperature limit $T \gg T_f$ where T_f is the Fermi temperature because in this limit spin channel is completely incoherent. Nevertheless, the spin incoherence persists into a much lower temperature scale T_0 below T_f . Although T_0 is a mean-field energy scale which does not mean the FM long-range order, it remains important roughly equal to the energy cost of flipping an individual electron spin in the ground state. Due to non-Gaussian fluctuations, the actual FM critical temperature T_c significantly deviates from T_0 defined in Eq. 1. In the current SU(2) invariant case, actually $T_c = 0$ due to the Mermin-Wagner theorem [57].

The compressibility $\kappa(T)$ reflects the coherence in the charge channel. Because the total particle number is a conserved quantity, it is also defined as an equal-time correlation function as

$$\kappa(T) = \lim_{L \rightarrow +\infty} \frac{\beta}{L^2} \sum_{\vec{r}_1, \vec{r}_2} \langle n(\vec{r}_1) n(\vec{r}_2) \rangle. \quad (9)$$

The QMC results of $\kappa(T)$ at $V = 0$ are presented in Fig. 1 (b). Again κ is proportional to $1/T$ in the high temperature incoherent regime as shown in Eq. 9, and it saturates at low temperatures in the metallic phase. The crossover temperature scale T_{ch} between these two regimes is typically the chemical potential at zero temperature. In the usual Fermi liquid state, κ is typically the density of state at the Fermi energy renormalized by Landau parameters. In our case, the situation is different due to the prominent FM fluctuations. At $V = 0$, due to the infinite U and the 1D band structure, T_{ch} is roughly the Fermi temperature of spinless fermions at the same density. For most values of n presented in Fig. 1 (b), T_{ch} is at the order of t_{\parallel} , and thus κ saturates in the temperature region presented. As for the case of a low hole density $n = 1.8$, T_{ch} can be estimated around 0.1, and thus $\kappa(T)$ does not saturate yet in the simulated temperature region. Because of the strong FM tendency, the inter-orbital interaction vanishes at $V = 0$ and $\kappa(T)$

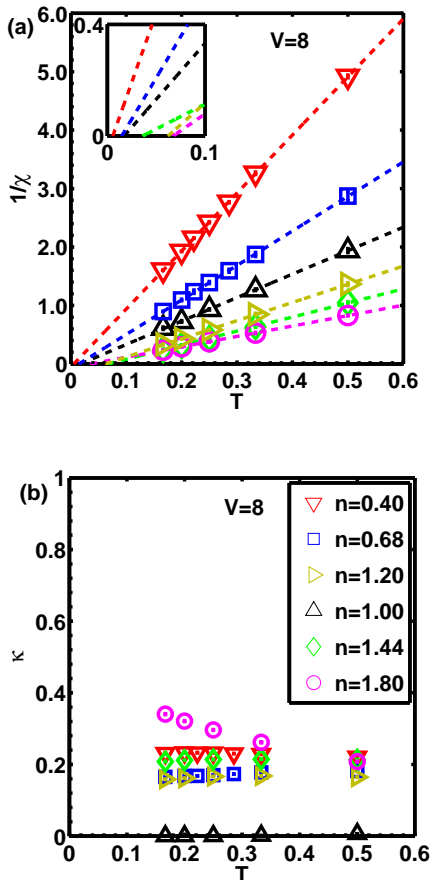


FIG. 2: (a) $\chi^{-1}(T)$ and (b) $\kappa(T)$ at a large value of $V = 8$ in the temperature regime of $1/6 < T < 1/2$. Different values of n are shown in the legend in (b). At $n = 1$, the system is in the Mott-insulating state, and thus $\kappa(T)$ drops to nearly zero at low temperatures. The error bars of the QMC data are smaller than the symbols.

can be well fitted by that of spinless fermions as shown in Fig. 1 (b).

Comparing $\chi(T)$ and $\kappa(T)$, the spin coherence temperature T_0 is much lower than the charge coherence temperature T_{ch} . These two distinct coherence temperature scales in spin and charge channels are an important feature of FM metals. A common phenomenological interpretation is to divide electrons into two parts: local moments and itinerant electrons which are responsible for the spin and charge channel behaviors, respectively. However, this dividing is artificial for metals when all the electrons are itinerant with equivalent band structures such as in our case. Based on the QMC simulations above, we have shown unambiguously that the CW-law can indeed appear in strongly correlated systems without local moment formation. A similar feature also appears in the CW metal states [67, 68] and the 1D spin incoherent Luttinger liquids [69]. The difference is the behavior of χ below the spin coherence temperature T_0 . In the

case of the CW-metal, χ saturates exhibiting the Pauli-like behavior but strongly enhanced by interactions, and in the 1D case, antiferromagnetic correlations develops. In our case, as will be shown in Fig. 6 in Sect. V, χ evolves into an exponential growth as a reminiscence of the FM long-range ordered ground state [21].

Next we consider the effects of a large inter-orbital repulsion V to $\chi^{-1}(T)$ and $\kappa(T)$. The ground states remain fully spin polarized as proved in Ref. [21], and the QMC results of $\chi^{-1}(T)$ still exhibit the CW law at all the fillings as shown in Fig. 2 (a). The most prominent effect of V is the suppression of $\kappa(T)$ at the commensurate filling of $n = 1$ as shown in Fig. 2 (b), in which the system is in the Mott-insulating state. In this case, electrons become local moments due to the opening of charge gap. As a result, $\kappa(T)$ is suppressed to nearly zero at $0 < T < 0.5$, which is still small compared to the charge gap at the order of V . In the Mott-insulating ground state at $n = 1$, the orbital channel can develop the antiferro-orbital ordering with a staggered occupation of p_x and p_y -orbitals. The QMC simulation results on the antiferro-orbital ordering transition are presented in Appendix C. As n moves away from 1, electrons become itinerant again. Nevertheless, the values of $\kappa(T)$ at $V = 8$ are significantly suppressed compared to those with the same values of n and T at $V = 0$.

B. The density dependences of $T_0(n)$ and the Curie constant $C(n)$

The ground state FM survives in all the filling region $0 < n < 2$, nevertheless, its robustness against thermal fluctuations varies at different densities, which reflects through the density dependences of $T_0(n)$ and $C(n)$.

The relation $T_0(n)$ is presented in Fig. 3 (a) for both cases of $V = 0$ and $V = 8$. The FM coherence is built up due to the itinerancy of fermions [21], thus T_0 approaches zero in both limits of $n \rightarrow 0$ (the particle vacuum) and $n \rightarrow 2$ (the hole vacuum). At $V = 0$, the maximal T_0 appears around $n = 1$ where electrons are most mobile. $T_0(n)$ at $V = 0$ is nearly symmetric with respect to $n = 1$ exhibiting an approximate particle-hole symmetry. In contrast, it is highly asymmetric at large V . In this case, T_0 is strongly suppressed at $0 < n < 1$, in which both charge and spin carriers are electrons. A large V penalizes two electrons occupying the same site, thus the effectiveness of Hund's rule is suppressed. After n passes 1, a quick increase of T_0 appears because extra electrons on top of the Mott background of $n = 1$ can move easily to build up the FM coherence. T_0 reaches the maximum roughly at the middle point between $n = 1$ and 2. As $n \rightarrow 2$, T_0 becomes insensitive to V . In this region, most sites are doubly occupied in the states of spin-1 moments, and holes are itinerant but do not carry spin. Hole's motion threads spin moments along its trajectory and aligns their orientations, and this process is not much affected by V . At $V = 8t_{||}$ and $J = 2t_{||}$, the

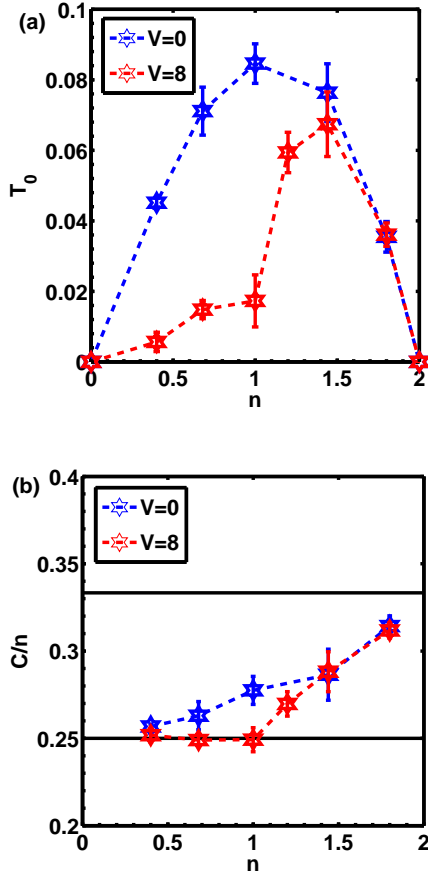


FIG. 3: (a) The density-dependence of the Curie temperature $T_0(n)$ at $V = 0$ and 8 with $J = 2$, respectively. (b) The density-dependence of the reduced Curie constant: C/n *v.s.* n . The lower and upper bold lines represent the limits of the spin- $\frac{1}{2}$ and spin-1 moments, respectively. Plots are based on the results of $\chi(T)$ in Fig. 1 (a) and Fig. 2 (a).

maximal $T_0 \approx 0.06t_{\parallel}$ which appears around $n \approx 1.4$. In other words, at large values of V , there is an approximate particle-hole symmetry between $n = 1$ to 2 on the background of one electron per site.

Next we present the results of the Curie constant C . Assuming the local moment picture, the simple molecule field method yields C per spin moment as $\frac{1}{3}S(S+1)$ [10], where S is the spin magnitude. In our case mostly itinerant, the magnitudes of S fluctuate: $C = 0$ for the empty site, $\frac{1}{4}$ for the singly occupied site, and $\frac{2}{3}$ for the doubly occupied site in the spin-1 configuration, respectively. We plot the normalized Curie constant C/n *v.s.* n in Fig. 3 (b). C/n approaches $\frac{1}{4}$ as $n \rightarrow 0$, and $\frac{1}{3}$ as $n \rightarrow 2$ where most sites are spin-1 moments. Generally, C/n lies between these two limits. At $V = 0$, as n increases, the number of onsite triplets smoothly increases and so does C/n . Nevertheless, at large V , the onsite triplet formation is strongly suppressed at $0 < n < 1$, and thus C/n is stuck at $\frac{1}{4}$. After n passes 1, C/n starts to increase nearly linearly toward $1/3$. As $n \rightarrow 2$, V hardly affects

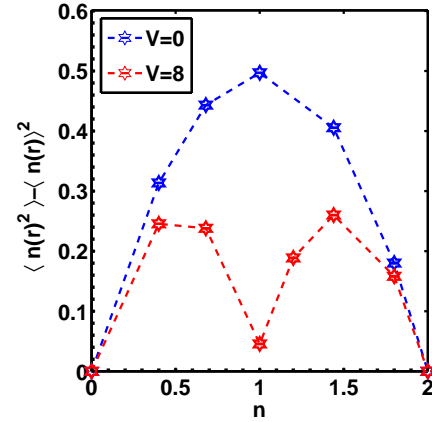


FIG. 4: The onsite particle number fluctuation δ defined in Eq. 10. The parameters $\beta = 6$, $J = 2$ and $L = 30$.

the number of onsite triplets, and thus C/n also becomes insensitive to V as T_0 does.

C. The onsite charge fluctuations and spin moments

To further clarify the nature of our system whether it is itinerant or local-moment-like, we calculate the onsite charge fluctuations and the average spin moments below. The onsite charge fluctuations are defined as

$$\delta = \langle n_i^2 \rangle - n^2, \quad (10)$$

where n_i is the total particle number on site i . Due to the translation symmetry, δ is independent of the site index i , and the simulation results are plotted in Fig. 4. At $V = 0$, the charge fluctuations are significant in the entire filling region except very close to the particle vacuum at $n = 0$ and the hole vacuum at $n = 2$. The maximum is reached at the approximate particle-hole symmetric point of $n = 1$. The large onsite charge fluctuations clearly reflect the itinerant nature of the system, which is consistent with the compressibility results in Fig. 1 (b). When the inter-orbital repulsion V goes large, charge fluctuations are greatly suppressed near the commensurate filling $n = 1$. In this case, the system becomes local-moment-like, which agrees with the vanishing compressibility shown in Fig. 2 (b). Nevertheless, as moving away from $n = 1$, the system becomes itinerant again exhibiting significant onsite charge fluctuations.

We also calculate the square of the z -component of the onsite spin moment $\langle S_{i,z}^2 \rangle$ which equals $\frac{1}{3}\langle \vec{S}_i^2 \rangle$ since the SU(2) symmetry is not broken. In order to compare with the Curie constant C/n , we plot its values normalized by the filling, i.e. $\langle S_{i,z}^2 \rangle / n$ as presented in Fig. 14 in Appendix B, which is nearly the same as the Curie constant C/n plotted in Fig. 3 (b). At $V = 0$, $\langle \vec{S}_i^2 \rangle$ varies

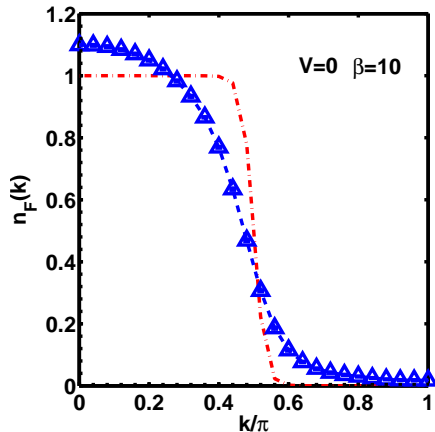


FIG. 5: The momentum space distribution $n_F(k)$ ($0 \leq k \leq \pi$) at $\beta = 10$ and $n = 1$, and $n_F(k)$ of the non-interacting spinless fermion (the red dashed line) is plotted for comparison. The system size $L = 50$. The parameter values are $V = 0$ and $J = 2$. The error bars of the QMC data are smaller than the symbol.

smoothly with n : the probable onsite configurations include empty, singly occupied (spin- $\frac{1}{2}$), and doubly occupied (spin-1) states. At $V = 8$ and the commensurate filling $n = 1$, $\langle \vec{S}_i^2 \rangle \approx \frac{3}{4}$, which manifests the formation of the local moment of spin- $\frac{1}{2}$ in consistent with the suppressed charge fluctuations. At $0 < n < 1$, each site is nearly either empty or singly occupied, and thus $\langle \vec{S}_i^2 \rangle \approx \frac{3}{4}n$. At $1 < n < 2$, the probable onsite configurations include the singly occupied spin- $\frac{1}{2}$ moment and doubly occupied spin-1 moment. Thus the system remains itinerant even in at large V when moving away from $n = 1$.

IV. THE MOMENTUM SPACE FERMION OCCUPATION

An important feature of the itinerant FM is the fluctuating FM domains in real space in the paramagnetic phase close to T_0 . This prominent FM fluctuations also strongly affect the momentum space fermion occupation as shown below. Basically, the fermion occupation functions still resemble those in the fully polarized systems with thermal broadening.

Because the particle number of each chain is separately conserved, the momentum space distribution function is essentially 1D-like. Nevertheless, each chain is not isolated but interacts with others through multi-orbital interactions, and thus spin is not conserved separately in each chain. Without loss of generality, we define $n_F(k) = \sum_{\sigma} \langle p_{x,\sigma}(k) p_{x,\sigma}(k) \rangle$ for a horizontal x -chain. The case of $n = 1$ is studied below as a representative, which is equivalent to $n_x = 0.5$ in this x -chain. Its mean-field Curie temperature $T_0 \approx 0.08$ as shown in Fig. 3 (a) before. The simulated results of $n_F(k)$ are presented in

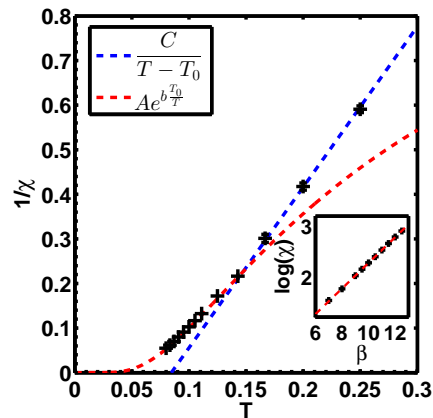


FIG. 6: The SU(2) invariant model in the critical region: $\chi^{-1}(T)$ at $n = 1$, $J = 2$ and $V = 0$. It crosses over from the CW law to the exponential form of $\chi(T) = Ae^{bT_0/T}$. The inset shows the linear scaling of $\ln \chi(T)$ v.s. β .

Fig. 5 with the periodical boundary condition, and a discussion on the boundary condition is presented in Appendix B.

We define a reference wavevector as the Fermi wavevector $k_f^0 = \frac{\pi}{2}$ of spinless fermions at the same density. At a low temperature $T = 1/\beta = 0.1$ close to T_0 , as shown in Fig. 5, $n_F(k)$ is only slightly larger than 1 even at $k \ll k_f^0$. It smoothly decays to zero with a half-width approximately equal to k_f^0 . $n_F(k)$ is rounded off compared to that of spinless fermions at the same temperature. Although $n_F(k)$ does not look much different from that of spinless fermions, it is a consequence of strong interactions because the system is in the paramagnetic state! The system remains unpolarized with a FM correlation length ξ at the order of $10 \sim 20$ as estimated in Appendix B, and the upper bound of $n_F(k) = 2$ as $k \rightarrow 0$.

The above result implies that the phase space for thermal fluctuations is not restricted to a small region close to $\pm k_f^0$, and thus its entropy capacity is enhanced. It is consistent with the real space picture of fluctuating FM domains as T approaches T_0 . This is highly non-perturbative showing the power of the QMC simulations.

V. THE LOW TEMPERATURE CRITICAL REGION

So far we have discussed the FM properties in the off-critical region. In this section we will further study the magnetic critical behavior through QMC. The FM order parameter is a conserved quantity, and thus there are no quantum fluctuations, however, in 2D thermal fluctuations are so strong that long-range FM ordering cannot appear at any finite temperatures for SU(2) symmetric models [57, 70]. Nevertheless, magnetic properties still

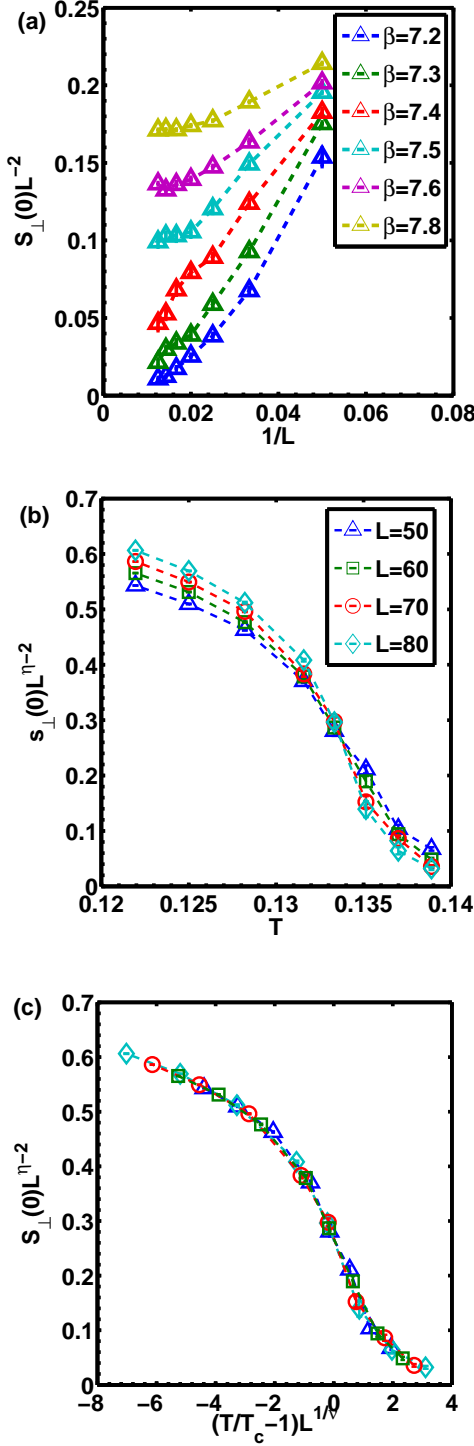


FIG. 7: The FM long-range ordering of the Ising symmetric model with parameters $J_{\perp} = 2J_{\parallel} = 4$, $n = 1$, and $V = 0$. (a) The finite size scaling of S_{\perp}/L^2 . The FM critical temperature is extracted as $T_c = 1/\beta_c = 0.134 \pm 0.002$ with $\beta_c \approx 7.4 \sim 7.5$. (b) The critical scaling: $S_{\perp}L^{-2+\eta}$ v.s. T with $\eta = \frac{1}{4}$. The crossing of curves at different values of L yields $T_c \approx 0.134$. (c) The data collapse of the scaling form $S_{\perp}(0)L^{-2+\eta} = f((T - T_c)L^{1/\nu})$ fitted by the parameters of $\nu = 1$, $\eta = \frac{1}{4}$ and $T_c = 0.1337$.

behave qualitatively differently in the off-critical and critical regions. We will also consider the model in the Ising class in which true FM long range ordering can appear, and determine the renormalized Curie temperature T_c .

In spite of the quasi-1D band structure, the magnetic properties of our model are intrinsically 2D because Hund's interaction couples spins of different chains together and the total spin of each chain is not separately conserved. In Fig. 6, we present the crossover of $\chi^{-1}(T)$ from the off-critical region to the critical region based on the finite size scaling presented in Appendix B. Although there is no distinct phase transition between the off-critical and critical regions, the temperature dependence of $\chi(T)$ changes qualitatively. The clear deviation from the CW law starts from $T \sim T_0 = 0.08$. In the critical region, the FM order parameter already develops a non-zero magnitude, and its directional fluctuations are described by the $O(3)$ non-linear σ -model. The FM correlation length increases exponentially as approaching zero temperature. $\chi(T)$ evolves to the exponential form fitted by $\chi = Ae^{b\frac{T_0}{T}}$ [71, 72], and the result in Fig. 6 shows $b = 3.1 \pm 0.3$ at $n = 1$, $V = 0$, and $J = 2$.

In order to obtain the FM long-range order, we modify Hund's coupling of Eq. 3 to reduce its symmetry from the $SU(2)$ to the Ising class: We introduce J_{\parallel} and J_{\perp} for the spin components in the xy -plane and along the z -direction, respectively, and choose $J_{\perp} > J_{\parallel}$. The z -component FM structure factor is defined as $S_{\perp}(T, L) = T\chi(T, L)$. For the case presented in Fig. 7 (a), the finite size scaling of $S_{\perp}(T, L)/L^2$ yields the critical temperature $T_c \approx 0.134$. This result is also checked from the scaling in the critical region in Fig. 7 (b) and (c). $S_{\perp}L^{-2+\eta}$ v.s. T is plotted with $\eta = \frac{1}{4}$ from the anomalous dimension of the 2D Ising universal class. The crossings of curves yield the value of T_c consistent with that of the previous scaling. Furthermore, a good data collapse is achieved by employing the scaling form

$$S_{\perp}L^{-2+\eta} = f((T - T_c)L^{\frac{1}{\nu}}) \quad (11)$$

with $\nu = 1$ of the 2D Ising class.

In Appendix D, the mean-field value $T_0 \approx 0.20$ is extracted based on the extrapolation of the CW behavior. Compared to the mean-field value T_0 , T_c is about 67% of T_0 as a result of the critical non-Gaussian fluctuations. For the 2D Ising model with only nearest neighbor coupling on the square lattice, the Onsager solution gives rise to $T_c = 2/\ln(\sqrt{2} + 1) \approx 2.269$ which is 57% of the Bragg-Williams mean-field results $T_0 = 4$. Thus the critical fluctuation strength of the case presented in Fig. 7 is weaker compared to that in the 2D Ising model in spite of the effect of the transverse component J_{\parallel} . This is due to the itinerant nature of our model such that the effective FM coupling is beyond two nearest neighboring sites.

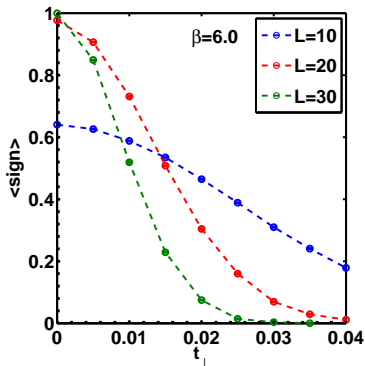


FIG. 8: The average of the fermion sign v.s. t_{\perp} at different values of L . The parameters are $V = 0$, $J = 2$, $n = 1$, and $\beta = 6$.

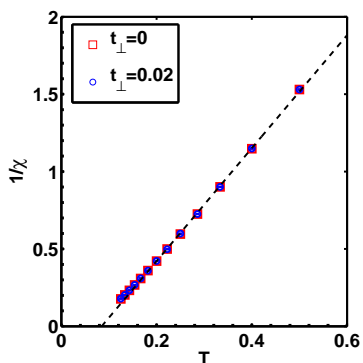


FIG. 9: $\chi^{-1}(T)$ at $t_{\perp} = 0$ and 0.02, respectively, with the system size $L = 20$. Periodical boundary conditions are used. The parameters are $V = 0$, $J = 2$, $n = 1$.

VI. DISCUSSIONS ON THE t_{\perp} -TERM AND THE FINITE U

In this section, we discuss the situations when the conditions for the absence of sign problem are loosed, including the presence of a small transverse hopping t_{\perp} -term as shown in Eq. 6, and the case of finite values of U .

A. QMC simulations with small transverse hopping term

The presence of the t_{\perp} -term enables electrons moving in the entire two-dimensional lattice, thus the fermion sign problem does appear. Nevertheless, the sign problem is not severe at small values of t_{\perp} , such that QMC simulations can still be performed. In Fig. 8, the average of sign is calculated from $t_{\perp} = 0$ to 0.05 at small and intermediate sample sizes with $\beta = 6$. We use the periodical boundary condition for the entire system, which is different from the boundary condition used in previous calculations in order to eliminate the sign problem

when electrons hop across the boundary. The previous boundary condition is feasible at $t_{\perp} = 0$ because particle number in each chain is conserved as explained in Sect. II B. Now under the periodical boundary condition, even at $t_{\perp} = 0$ the sign is not positive definite: when one electron hops across the boundary, if the fermion number in that chain is an even number, the matrix element acquires an extra sign. This boundary effect is more prominent at small sample sizes (e.g. $L = 10$) but already becomes negligible at intermediate sample sizes, say, $L > 20$. As t_{\perp} deviates from 0, the 2D motion of electrons suppresses the average sign and it drops more rapidly at larger sample sizes.

We have simulated the spin susceptibility and presented its inverse $\chi^{-1}(T)$ in Fig. 9 with $t_{\perp} = 0.02$. The results at $t_{\perp} = 0$ under the periodical boundary condition are also plotted for a comparison. An intermediate sample size ($L = 20$) is used and the simulation is performed from the high to intermediate temperature regions. The results at $t_{\perp} = 0.02$ are nearly the same as those at $t_{\perp} = 0$, which still exhibit the CW behavior. At the lowest temperature simulated $\beta = 6$, the average sign at $t_{\perp} = 0.02$ is already significantly below 1. Nevertheless, the difference between $\chi^{-1}(T)$'s at $t_{\perp} = 0$ and 0.02 remains negligible. These results show that the magnetic properties are not so sensitive to t_{\perp} when $t_{\perp}/t_{\parallel} \ll 1$.

Certainly, when t_{\perp} reaches the same order as t_{\parallel} , the band structure will become genuinely two-dimensional. In this case, the previous ground FM theorem does not apply, and a quantum phase transition is likely to occur from the FM to paramagnetic ground states. Unfortunately, the sign problem will be very severe and thus reliable QMC simulations cannot be performed. It would be interesting to further develop other analytic and numeric methods to investigate this problem.

B. The effect of the finite U

As explained in Sect. II B, the many-body bases for simulations, which are also used for the proof of FM ground state theorems in Ref. [21], are constructed by ordering electrons according to their locations along one chain by another regardless of their spin configurations. This set of bases are convenient to accommodate to the spin-flip term of Hund's coupling to be free of the sign problem, nevertheless, finite U does cause this problem. If U is finite, states with doubly occupied orbitals are allowed, and electrons with opposite spins can exchange their locations which causes the sign problem. We will defer the QMC simulations for this case to a later publication, but briefly analyze the physical effect below.

Basically, a large but finite U introduces an antiferromagnetic (AFM) energy scale of $J_{AF} = 4t_{\parallel}^2/U$ for two electrons lying in adjacent sites in the same chain. Its effect in the low electron density region is unimportant but becomes important in the limit of $n \rightarrow 2$ in which most sites are occupied as spin-1 moments. In this region,

the FM energy scale $T_0(n)$ is suppressed because of the low density of mobile holes and finally it becomes weaker than J_{AF} . Consequently, we expect a ground state phase transition at a critical density n_c close to $n = 2$, which marks a transition from the FM ordering at $n < n_c$ to the AFM ordering at $n_c < n < 2$.

VII. EXPERIMENT REALIZATIONS

The QMC simulations presented above are not only of academic interests but also provide new directions to explore new FM materials in various physical systems, including both the ultra-cold atom optical lattices and the strongly correlated transition metal oxides.

Recently, the study of itinerant FM states has become a research focus in ultra-cold cold atom physics [24–31]. However, so far it is still in debate whether the experiment results based on the upper branches of the Feshbach resonances have shown the existence of itinerant FM or not. Our work suggests a new direction for the further experiment exploration of itinerant FM in the high orbital bands in optical lattices. Our band Hamiltonian can be accurately implemented in the p -orbital band in the ultra-cold atom optical lattices [73–75]. Due to the anisotropy of p -orbital orientation, the transverse π -bonding amplitude t_\perp is usually much smaller than the longitudinal σ -bonding t_\parallel . The ratio of t_\perp/t_\parallel decreases as increasing the optical potential depth V_0 . As shown in Ref. [73], as $V_0/E_R = 15$ where E_R is the recoil energy of the laser forming the optical lattice, $t_\perp/t_\parallel \approx 5\%$, such that we can neglect the t_\perp term in Eq. 2. Furthermore, the interaction strength is also tunable in optical lattices by simply varying laser intensities, and the strong coupling regime can be reached. A variation study based on the Gutzwiller projection also shows that the ground state FM may start from intermediate coupling strength [75]. Our simulations on the thermodynamic properties provide important guidance for future experiments.

Our work is also helpful for the current effort of searching for novel FM materials in transition metal oxides, in particular, in systems with the t_{2g} -orbital bands, i.e., d_{xz} , d_{yz} , and d_{xy} bands, with the quasi-2D layered structure. In fact, FM has been observed experimentally in the (001) interface of 3d-orbital transition-metal oxides such as SrTiO₃/LaAlO₃ [20, 76–79], which has been a recent research focus in condensed matter physics. The dispersions of d_{xz} and d_{yz} -orbital bands are also highly anisotropic, i.e., the longitudinal bonding parameter t_\parallel is much larger than the transverse one t_\perp , as described in Eq. 2 by replacing $p_{x(y)}$ with $d_{x(y)z}$. The onsite repulsive interaction of the 3d-electrons are particularly strong, such that the projection of doubly occupied orbitals is a good approximation.

Even though there is an additional quasi 2D- d_{xy} -orbital band in the SrTiO₃/LaAlO₃ interfaces, which is presumably paramagnetic by itself, it is conceivable that the overall system remains FM as shown in experiments

and our results still apply qualitatively. The reason is that the quasi-1D bands $d_{x(y)z}$ do not hybridize with the quasi-2D d_{xy} band by the nearest neighboring hopping due to their different parity eigenvalues under the reflections with respect to xy , yz and zx -planes, respectively. It is a good approximation that the particle numbers in the d_{xy} -band and in the $d_{x(y)z}$ bands are separately conserved, and they only couple through interactions. The coupling is ferromagnetic by nature due to Hund's rule. Since the quasi-1D bands by themselves are already FM in the strong coupling regime, their coupling to the paramagnetic d_{xy} -band is like to use a permanent ferromagnet to polarize a paramagnet, and it is conceivable that in overall the ferromagnetism is enhanced.

VIII. CONCLUSIONS

In summary, we have non-perturbatively investigated the thermodynamic properties of an unambiguous itinerant FM system with multi-orbital structures through the method of the SSE QMC. The simulations are proved to be sign problem free in all the electron density region, and thus reliable numerical results can be obtained at high numeric accuracy. Due to the nature of asymptotic exactness of our simulations, they provide a solid reference point for the study of the strong correlation effects of the thermodynamic properties of itinerant FM systems. There is a wide temperature region $T_0 < T < T_{ch}$, in which the spin channel is incoherent without local moments existing as a priori, while the charge channel exhibits the metallic behavior. The spin magnetic susceptibility exhibits the CW law in the off-critical region as a result of strong correlations. It further crosses over to the exponential growth in the critical region. The compressibility is weakly temperature dependent and saturates to its zero temperature value. The true FM long-range transition appears when the symmetry class is reduced from SU(2) to Ising. The finite size scaling in the critical region gives rise to an accurate determination of the FM transition temperature. Our work is also closely related to the experiment efforts of searching for novel FM states of matter in both ultra-cold atom optical lattices and in the 3d transition metal oxide materials.

Acknowledgments

C. W. is grateful for the hospitality of Center of Mathematical Sciences and Applications at Harvard University where part of the work was done. S. X. and C. W. are supported by the NSF DMR-1410375 and AFOSR FA9550-14-1-0168. Y. L. is grateful for the support from the Princeton Center for Theoretical Science. S. X., Y. L. and C. W. thank D. Arovass, X. Dai, J. E. Hirsch, M. Randeria, A. W. Sandvik, H. Shao, L. J. Sham, D. J. Singh, N. Trivedi, and Lu Yu for helpful discussions. All the simulation was performed on Tiger Cluster in Prince-

ton. C. W. acknowledges the support from the National Natural Science Foundation of China (11328403), and the support from the Presidents Research Catalyst Awards of University of California. Y. L. thanks the hospitality of the Aspen Center of physics under the support of the NSF Grant No. PHYS-1066293.

Appendix A: Parameters for QMC simulations

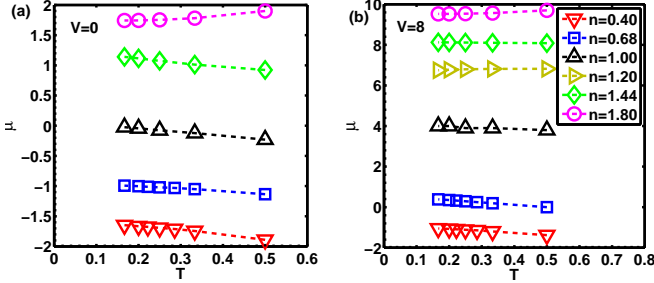


FIG. 10: The chemical potential $\mu(T)$ is tuned to maintain the filling n unchanged at all temperatures. The system size is $L = 8$.

We have used SSE method of QMC to simulate the Hamiltonian Eq. 2 plus Eq. 3 in the main text with the directed loop algorithm [62–66]. A Monte Carlo step is defined as a diagonal vertex update followed by many directed off-diagonal loop updates to ensure that most of vertex legs are visited by the worm-head. The simulated system size of the square lattice is $L \times L$ with the values of L given in each figure. The simulations are run in parallel on 16 cores. On each core 1.5×10^5 warm-up steps are used, and for a typical data point we use 10^5 QMC steps and perform 10^4 measurements. For the simulation with the largest system size ($L = 80$), 3.0×10^5 warm-up steps and 2.0×10^5 QMC steps are used.

In order to maintain ergodicity, the directed loop algorithm is carried out in the grand canonical ensemble in which the chemical potential μ is the characteristic variable. Nevertheless, in realistic systems, it is more natural to fix the average fermion number per site n rather than to fix μ . For example, in a system with a fixed average value of n , $\mu(T)$ changes as varying the temperature T . Therefore, in presenting the simulation results for a fixed value of n , we have carefully adjusted μ to maintain n invariant. The obtained relations of $\mu(T)$ at various values of n with the system size $L = 8$ are plotted in Fig. 10. The dependence of μ on L is weak, and thus we use the same set values of $\mu(T)$ for even larger sample sizes except the case of $V = 0$ and $n = 0.40$. In this case, the finite size effect of μ is relatively strong, and we calculate $\mu(T)$ at $L = 10$ and use it for larger sample sizes. By this method, we can maintain the values of n invariant within the error of $\Delta n = 0.006$ for all the simulations.

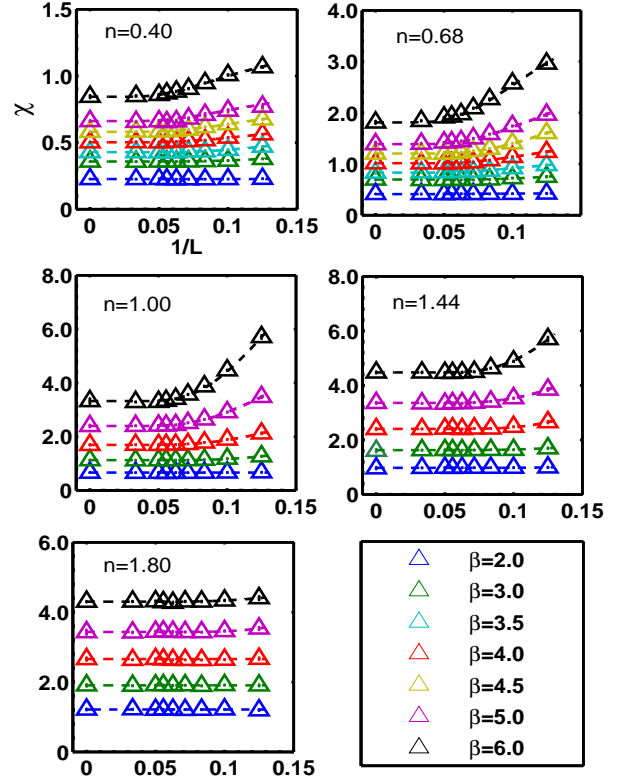


FIG. 11: The finite size scalings for $\chi(T, L)$ v.s. $1/L$ with the fitting $\chi(T, L) = aLe^{-L/b} + \chi(T)$. Values of $\beta = 1/T$ are presented in the legend. The parameter value at $V = 0$ and $J = 2$.

Appendix B: More information on thermodynamic properties

In Fig. 11 and Fig. 12, the finite size scaling of $\chi(T, L)$ are plotted with $J = 2$ at $V = 0$ and $V = 8$, respectively. In both cases, curves are fitted with the scaling ansatz $\chi(L, T) = \chi_0(T) + aLe^{-L/b}$ to extrapolate the spin susceptibility $\chi(T)$ for the infinite system size. For the data sets with $\beta < 6$, we have simulated lattice sizes $L \times L$ up to $L = 30$.

In Fig. 13, we present the finite size scaling of $\chi(T, L)$ in the critical region with β from 7 to 12.5 and with parameters $V = 0$, $J = 2$ and $n = 1$. The extrapolated values of $\chi(T)$ are used in Fig. 3 (a) in the main text. Let us look at the curve with $\beta = 10$, the dependence of $\chi(T, L)$ on L converges at large values of L . The starting of convergence takes places at values of L at the order from 10 to 20, and thus we estimate the FM correlation length ξ at $\beta = 10$ also in this range.

In Fig. 14, we plot the QMC simulation results for the onsite spin moment square normalized by filling density $\langle S_z^2 \rangle / n$, which behaves nearly the same as the Curie constants presented in Fig. 3 (b). Due to the SU(2) symmetry, the onsite spin moment square $\langle S^2 \rangle / n = 3 \langle S_z^2 \rangle / n$. A discussion on $\langle S_z^2 \rangle / n$ is presented in the Sect. III C.

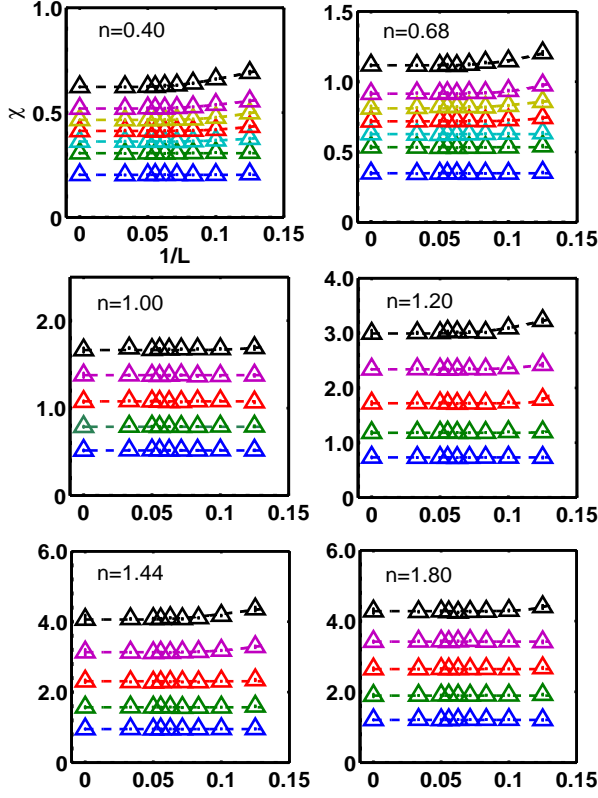


FIG. 12: The finite size scaling of $\chi(T, L)$ v.s. $1/L$ for $V = 8$. Scaling ansatz $\chi(T, L) = aLe^{-\frac{L}{T}} + \chi(T)$ is used. The legend is the same as that in Fig. 11.

Next we discuss the momentum space distribution $n_F(k)$ which is 1D-like because the particle number of each chain is separately conserved. Due to this feature, we make a special choice of boundary conditions to remove the sign problem: the periodical (anti-periodical) boundary condition for a chain if its particle number is odd (even). Our simulation uses the grand canonical assemble, and thus both configurations with even and odd particle numbers are sampled which can also be easily distinguished. For configurations with odd particle numbers, the values of k take $2p\pi/L$ with $p = 0, \pm 1, \dots, \pm(L-1)$, and for configurations with even particle numbers, the values of k take $2p\pi/L$ with $p = \pm\frac{1}{2}, \dots, \pm(L-\frac{1}{2})$. Because of this reason, we simulate $n_F(k)$ by separately sampling configurations of even and odd particle numbers and present both of them in Fig. 15 (a) and (b), respectively. Results of the sample sizes with $L = 30$ and 50 are presented, which shows that the finite size dependence is very weak. At both sample sizes $L = 30$ and 50 , the differences caused by using periodical or anti-periodical boundary conditions are rather small. And the result under the periodical boundary condition is presented Fig. 1c in the main text.

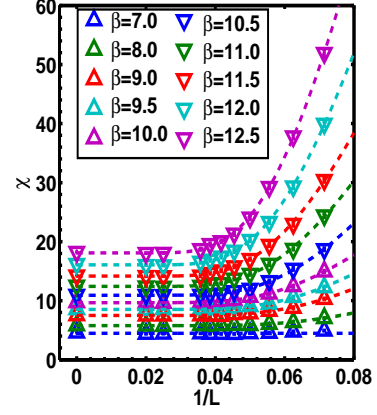


FIG. 13: The finite size scaling of $\chi(T, L)$ at $n = 1$, $V = 0$, and $J = 2$ in the low temperature critical region with the scaling ansatz $\chi(T, L) = aLe^{-\frac{L}{T}} + \chi(T)$ used. Values of $\beta = 1/T$ are presented in the legend.

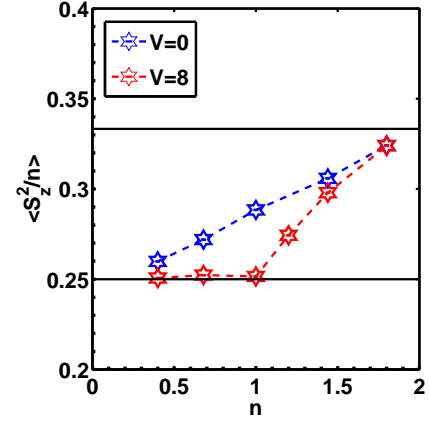


FIG. 14: The QMC results for the normalized onsite spin moment $\langle S_z^2 \rangle/n$ at $\beta = 6$, $J = 2$, and $L = 30$. Values of V are marked in the inset.

Appendix C: The orbital ordering at the commensurate filling $n = 1$

Here we present the QMC simulations on the orbital ordering with a large value of the inter-orbital repulsion V . Large V suppresses doubly occupied on-site states, and at the commensurate filling $n = 1$, the ground state is in the Mott-insulating state. In this case, fermions become local moments. At zero temperature, even though electron spins are fully polarized, the orbital degree of freedom enables the superexchange in the orbital channel [80]. The orbital exchange is described by an antiferro-orbital Ising model

$$H_{ex} = J_{orb} \sum_{\vec{r}, \vec{r}'} \tau_z(\vec{r}) \tau_z(\vec{r}'), \quad (C1)$$

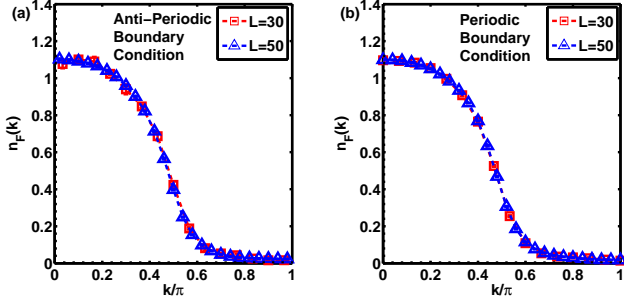


FIG. 15: The momentum space occupation $n_F(k)$ at $\beta = 10$, $V = 0$, $J = 2$ and $n = 1$. Results of $n_F(k)$ for both the anti-periodical boundary condition and the periodical boundary condition are presented at two different sizes of $L = 30$ and 50 .

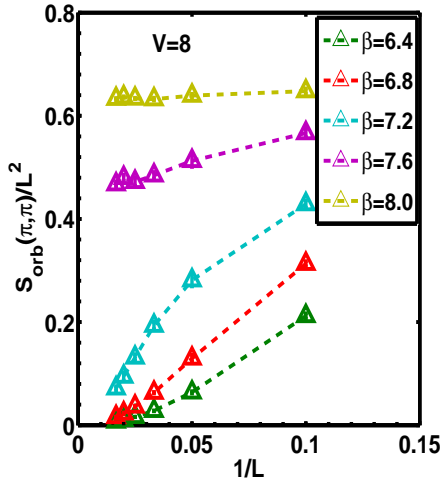


FIG. 16: The finite size scaling of $S_{orb}(\pi, \pi)/L^2$ with the parameter values $J_{\perp} = J_{\parallel} = 2$, $n = 1$ and $V = 8$. The system sizes range from $L = 10$ to 60 and the values of inverse temperature β are presented in the legend. The orbital ordering occurs at β between 7.2 to 7.6 , which corresponds to $T_{orb}/t_{\parallel} \approx 0.132 \sim 0.139$.

where $J_{orb} = t_{\parallel}^2/V$ and $\tau_z = p_x^{\dagger}p_x - p_y^{\dagger}p_y$. At low temperatures, due to the prominent FM tendency, the above orbital exchange model still applies, thus below the temperature scale around J_{orb} , the antiferro-orbital ordering, i.e., the staggered occupation of p_x and p_y -orbitals, will appear.

We define the equal-time orbital structure factor as:

$$S_{orb}(\vec{q}, \tau) = \frac{1}{L^2} \sum_{\vec{r}_1, \vec{r}_2} \langle m_{orb}(\vec{r}_1, \tau) m_{orb}(\vec{r}_2, \tau) \rangle e^{i\vec{q} \cdot (\vec{r}_2 - \vec{r}_1)}, \quad (C2)$$

where $m_{orb}(\vec{r}, \tau) = n_x(\vec{r}, \tau) - n_y(\vec{r}, \tau)$ is the on-site orbital polarization. Since the orbital ordering occurs at the wavevector (π, π) , we present the QMC simulation

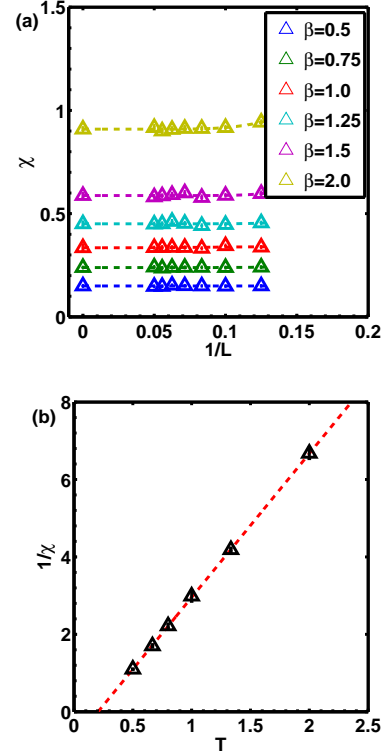


FIG. 17: (a) The finite size scaling of $\chi(T, L)$ v.s. $1/L$ in the off-critical region. The Hund's rule coupling is modified as $J_{\perp} = 2J_{\parallel} = 4$. (b) The CW behavior of the extrapolated $\chi^{-1}(T)$. The interception on the temperature axis yields $T_0/t_{\parallel} = 0.20 \pm 0.01$.

of the finite scaling of $S_{orb}(\pi, \pi)/L^2$ in Fig. 16. It indicates that the antiferro-orbital ordering appears at low temperatures, and the critical temperature T_{orb}/t_{\parallel} lies between 0.132 and 0.139 .

Appendix D: QMC simulations for the Ising class Hamiltonian

For the Ising class Hamiltonian with the modified Hund's coupling with $J_{\perp} = 2J_{\parallel} = 4$, we extract its mean-field value of the Curie temperature T_0 following the method presented in the main text. The spin susceptibility $\chi(T)$ is obtained after the finite size scaling for $\chi(T, L)$ in the off-critical region as shown in Fig. 17 (a). By the linear extrapolation of $\chi^{-1}(T)$ in the off-critical region, we obtain T_0 from the interception of $\chi^{-1}(T)$ on the temperature axis as shown in Fig. 17 (b). The scaling is performed in the region $T > 0.5$ below which the deviation from the CW behavior appears. The linear extrapolation of $\chi^{-1}(T)$ gives rise to $T_0 = 0.20 \pm 0.01$. The magnetic structure factors at even lower temperatures in the critical region are presented in Fig. 7 in the main text.

-
- [1] E. C. Stoner. Collective electron ferromagnetism. *Proc. R. Soc. Lond. A*, 169(938):339, 1938.
- [2] Clarence Zener. Interaction between the d -shells in the transition metals. ii. ferromagnetic compounds of manganese with perovskite structure. *Phys. Rev.*, 82:403–405, May 1951.
- [3] J. C. Slater. Ferromagnetism and the band theory. *Rev. Mod. Phys.*, 25:199–210, Jan 1953.
- [4] P. W. Anderson and H. Hasegawa. Considerations on double exchange. *Phys. Rev.*, 100:675–681, Oct 1955.
- [5] Elliott H. Lieb and Daniel Mattis. Theory of ferromagnetism and the ordering of electronic energy levels. *Phys. Rev.*, 125:164–172, Jan 1962.
- [6] Yosuke Nagaoka. Ferromagnetism in a narrow, almost half-filled s band. *Phys. Rev.*, 147:392–405, Jul 1966.
- [7] C. Herring. *Magnetism*. Academic, Berlin, 1966.
- [8] John A. Hertz. Quantum critical phenomena. *Phys. Rev. B*, 14(3):1165–1184, Aug 1976.
- [9] K. K. Murata and S. Doniach. Theory of magnetic fluctuations in itinerant ferromagnets. *Phys. Rev. Lett.*, 29:285–288, Jul 1972.
- [10] Tôru Moriya. *Spin Fluctuations in Itinerant Electron Magnetism*, volume 56 of *Springer Series in Solid-State Sciences*. Springer, Berlin Heidelberg, 1985.
- [11] J. E. Hirsch. Metallic ferromagnetism in a single-band model. *Phys. Rev. B*, 40:2354–2361, Aug 1989.
- [12] Andreas Mielke and Hal Tasaki. Ferromagnetism in the hubbard model—examples from models with degenerate single-electron ground states. *Commun. Math. Phys.*, 158:341, 1993.
- [13] Hal Tasaki. Ferromagnetism in the hubbard models with degenerate single-electron ground states. *Phys. Rev. Lett.*, 69:1608–1611, Sep 1992.
- [14] A. J. Millis. Effect of a nonzero temperature on quantum critical points in itinerant fermion systems. *Phys. Rev. B*, 48(10):7183–7196, Sep 1993.
- [15] K. Baberschke, W. Noth, and M. Donath, editors. *Band-Ferromagnetism*. Springer-Verlag, Berlin, 2001.
- [16] D. Belitz, T. R. Kirkpatrick, and Thomas Vojta. How generic scale invariance influences quantum and classical phase transitions. *Rev. Mod. Phys.*, 77:579–632, Jul 2005.
- [17] J. Jackiewicz and K. S. Bedell. Quantum fluctuation driven first-order phase transition in weak ferromagnetic metals. *Philosophical Magazine*, 85:1755–1763, June 2005.
- [18] Hilbert v. Löhneysen, Achim Rosch, Matthias Vojta, and Peter Wölfle. Fermi-liquid instabilities at magnetic quantum phase transitions. *Rev. Mod. Phys.*, 79:1015–1075, Aug 2007.
- [19] Dmitrii L. Maslov and Andrey V. Chubukov. Nonanalytic paramagnetic response of itinerant fermions away and near a ferromagnetic quantum phase transition. *Phys. Rev. B*, 79:075112, Feb 2009.
- [20] Gang Chen and Leon Balents. Ferromagnetism in itinerant two-dimensional t_{2g} systems. *Phys. Rev. Lett.*, 110:206401, May 2013.
- [21] Yi Li, Elliott H. Lieb, and Congjun Wu. Exact results for itinerant ferromagnetism in multi-orbital systems on square and cubic lattices. *Phys. Rev. Lett.*, 112:217201, May 2014.
- [22] Y. Sang, D. Belitz, and T. R. Kirkpatrick. Disorder dependence of the ferromagnetic quantum phase transition. *arXiv:1406.5745*, June 2014.
- [23] Daniel C. Mattis. *The Theory of Magnetism Made Simple*. World Scientific, Singapore, 2006.
- [24] R. A. Duine and A. H. MacDonald. Itinerant ferromagnetism in an ultracold atom fermi gas. *Phys. Rev. Lett.*, 95:230403, 2005.
- [25] G.-B. Jo, Y.-R. Lee, J.-H. Choi, C. A. Christensen, T. H. Kim, J. H. Thywissen, D. E. Pritchard, and W. Ketterle. Itinerant Ferromagnetism in a Fermi Gas of Ultracold Atoms. *Science*, 325:1521–, September 2009.
- [26] Shizhong Zhang, Hsiang-hsuan Hung, and Congjun Wu. Proposed realization of itinerant ferromagnetism in optical lattices. *Phys. Rev. A*, 82:053618, Nov 2010.
- [27] I. Berdnikov, P. Coleman, and S. H. Simon. Itinerant ferromagnetism in an atom trap. *Phys. Rev. B*, 79(22):224403, June 2009.
- [28] D. Pekker and E. Demler. Competing instabilities in quench experiments with ultracold Fermi gases near a Feshbach resonance. *arXiv:1107.3930*, July 2011.
- [29] Chia-Chen Chang, Shiwei Zhang, and David M. Ceperley. Itinerant ferromagnetism in a fermi gas with contact interaction: Magnetic properties in a dilute hubbard model. *Phys. Rev. A*, 82:061603, Dec 2010.
- [30] Xiaoling Cui and Tin-Lun Ho. Ground-state ferromagnetic transition in strongly repulsive one-dimensional fermi gases. *Phys. Rev. A*, 89:023611, Feb 2014.
- [31] S. Pilati, I. Zintchenko, and M. Troyer. Ferromagnetism of a repulsive atomic fermi gas in an optical lattice: A quantum monte carlo study. *Phys. Rev. Lett.*, 112:015301, Jan 2014.
- [32] W. Kohn and L. J. Sham. Self-consistent equations including exchange and correlation effects. *Phys. Rev.*, 140:A1133–A1138, Nov 1965.
- [33] U. V. Barth and L. Hedin. A local exchange-correlation potential for the spin polarized case. i. *J. Phys. C: Solid State Phys.*, 5:1629, 1972.
- [34] V. L. Moruzzi, J. F. Janak, and A. R. Williams. *Calculated Electronic Properties of Metals*. Pergamon Press Inc., 1978.
- [35] B. Himmetoglu, A. Floris, S. de Gironcoli, and M. Cococcioni. Hubbard-corrected DFT energy functionals: the LDA+U description of correlated systems. *arXiv:1309.3355*, September 2013.
- [36] Antoine Georges, Gabriel Kotliar, Werner Krauth, and Marcelo J. Rozenberg. Dynamical mean-field theory of strongly correlated fermion systems and the limit of infinite dimensions. *Rev. Mod. Phys.*, 68:13–125, Jan 1996.
- [37] E. Gull, A. J. Millis, A. I. Lichtenstein, A. N. Rubtsov, M. Troyer, and P. Werner. Continuous-time Monte Carlo methods for quantum impurity models. *Rev. Mod. Phys.*, 83:349–404, April 2011.
- [38] K. Held, I. A. Nekrasov, G. Keller, V. Eyert, N. Blümer, A. K. McMahan, R. T. Scalettar, T. Pruschke, V. I. Anisimov, and D. Vollhardt. The LDA+DMFT Approach to Materials with Strong Electronic Correlations. *eprint arXiv:cond-mat/0112079*, December 2001.
- [39] Martin C. Gutzwiller. Effect of correlation on the ferromagnetism of transition metals. *Phys. Rev. Lett.*, 10:159–162, Mar 1963.
- [40] Jia Ning Zhuang, Lei Wang, Zhong Fang, and Xi Dai.

- Fast impurity solver based on gutzwiller variational approach. *Phys. Rev. B*, 79:165114, Apr 2009.
- [41] W. Weber, J. Bünemann, and F. Gebhard. *Band-Ferromagnetism*. Springer-Verlag, Berlin, 2001.
- [42] B. S. Shastry, H. R. Krishnamurthy, and P. W. Anderson. Instability of the nagaoka ferromagnetic state of the $u = \infty$ hubbard model. *Phys. Rev. B*, 41:2375–2379, Feb 1990.
- [43] Guang-Shan Tian. Stability of the nagaoka state in the one-band hubbard model. *Phys. Rev. B*, 44:4444–4448, Sep 1991.
- [44] Hal Tasaki. Extension of nagaoka’s theorem on the large- U hubbard model. *Phys. Rev. B*, 40:9192–9193, Nov 1989.
- [45] Li Liu, Hong Yao, Erez Berg, Steven R. White, and Steven A. Kivelson. Phases of the infinite $\frac{1}{2}$ hubbard model on square lattices. *Phys. Rev. Lett.*, 108:126406, Mar 2012.
- [46] Z.-C. Gu, H.-C. Jiang, and G. Baskaran. Emergence of $\frac{1}{2}$ superconductivity in $\frac{1}{2}$ strongly correlated Dirac fermions. *arXiv:1408.6820*, August 2014.
- [47] Andreas Mielke. Ferromagnetic ground states for the hubbard model on line graphs. *J. Phys. A: Math. Gen.*, 24(2):L73, 1991.
- [48] Tru Moriya and Arisato Kawabata. Effect of spin fluctuations on itinerant electron ferromagnetism. *Journal of the Physical Society of Japan*, 34(3):639–651, 1973.
- [49] Joachim Stoeck and Hans Christoph Siegmann. *Magnetism, From Fundamentals to Nanoscale Dynamics*. Springer, 2006.
- [50] P Fazekas. *Lecture Notes on Electron Correlation and Magnetism*. Series in Modern Condensed Matter Physics. World Scientific Pub Co Inc, 1999.
- [51] P. Rhodes and E. P. Wohlfarth. The effective curie-weiss constant of ferromagnetic metals and alloys. *Proc. R. Soc. Lond. A*, 273:247–258, 1962.
- [52] J. E. Hirsch. Metallic ferromagnetism in a single-band model. ii. finite-temperature magnetic properties. *Phys. Rev. B*, 40:9061–9069, Nov 1989.
- [53] C. Aron and G. Kotliar. Analytic theory of Hund’s metals: a renormalization group perspective. *arXiv:1401.0331*, January 2014.
- [54] Luca de Medici, S. R. Hassan, Massimo Capone, and Xi Dai. Orbital-selective mott transition out of band degeneracy lifting. *Phys. Rev. Lett.*, 102:126401, Mar 2009.
- [55] V. I. Anisimov, I. A. Nekrasov, D. E. Kondakov, T. M. Rice, and M. Sgrist. Localization in ruthenates: magnetic and electronic properties of $\text{Ca}_{2-x}\text{Sr}_x\text{RuO}_4$. *Eur. Phys. J. B*, 25:191, 2002.
- [56] A. I. Lichtenstein, M. I. Katsnelson, and G. Kotliar. Finite-temperature magnetism of transition metals: An *ab initio* dynamical mean-field theory. *Phys. Rev. Lett.*, 87:067205, Jul 2001.
- [57] N. D. Mermin and H. Wagner. Absence of Ferromagnetism or Antiferromagnetism in One- or Two-Dimensional Isotropic Heisenberg Models. *Phys. Rev. Lett.*, 17(22):1133–1136, November 1966.
- [58] Laura M. Roth. Simple narrow-band model of ferromagnetism due to intra-atomic exchange. *Phys. Rev.*, 149:306–308, Sep 1966.
- [59] KI Kugel and DI Khomskii. Crystal structure and magnetic properties of substances with orbital degeneracy. *Zh. Eksp. Teor. Fiz*, 64:1429–1439, 1973.
- [60] M. Cyrot and C. Lyon-Caen. Orbital superlattice in the degenerate hubbard model. *J. Phys. France*, 36(3):253–266, 1975.
- [61] A. M. Oleś. Antiferromagnetism and correlation of electrons in transition metals. *Phys. Rev. B*, 28:327–339, Jul 1983.
- [62] Anders W. Sandvik and Juhani Kurkijärvi. Quantum monte carlo simulation method for spin systems. *Phys. Rev. B*, 43:5950–5961, Mar 1991.
- [63] Naoki Kawashima and Kenji Harada. Recent developments of world-line monte carlo methods. *Journal of the Physical Society of Japan*, 73(6):1379–1414, 2004.
- [64] Bernard Borodol Beard and U-J Wiese. Simulations of discrete quantum systems in continuous euclidean time. *Physical review letters*, 77(25):5130, 1996.
- [65] Pinaki Sengupta, Anders W Sandvik, and David K Campbell. Bond-order-wave phase and quantum phase transitions in the one-dimensional extended hubbard model. *Physical Review B*, 65(15):155113, 2002.
- [66] Olav F. Syljuåsen and Anders W. Sandvik. Quantum Monte Carlo with directed loops. *Phys. Rev. E*, 66(4):046701, October 2002.
- [67] Maw Lin Foo, Yayu Wang, Satoshi Watauchi, H. W. Zandbergen, Tao He, R. J. Cava, and N. P. Ong. Charge ordering, commensurability, and metallicity in the phase diagram of the layered Na_xCoO_2 . *Phys. Rev. Lett.*, 92:247001, Jun 2004.
- [68] J. Merino, B. J. Powell, and Ross H. McKenzie. Ferromagnetism, paramagnetism, and a curie-weiss metal in an electron-doped hubbard model on a triangular lattice. *Phys. Rev. B*, 73:235107, Jun 2006.
- [69] Gregory A. Fiete. Colloquium. *Rev. Mod. Phys.*, 79:801–820, Jul 2007.
- [70] T. A. Zaleski and T. K. Kopeć. Néel order in the hubbard model within a spin-charge rotating reference frame approach: Crossover from weak to strong coupling. *Phys. Rev. B*, 77:125120, Mar 2008.
- [71] Daniel P. Arovas and Assa Auerbach. Functional integral theories of low-dimensional quantum heisenberg models. *Phys. Rev. B*, 38:316–332, Jul 1988.
- [72] Minoru Takahashi. Classical heisenberg ferromagnet in two dimensions. *Phys. Rev. B*, 36:3791–3797, Sep 1987.
- [73] A. Isacsson and S. M. Girvin. Multi-flavor bosonic Hubbard models in the first excited Bloch band of an optical lattice. *Phys. Rev. A*, 72:053604, 2005.
- [74] W. V. Liu and C. Wu. Atomic matter of nonzero-momentum bose-einstein condensation and orbital current order. *Phys. Rev. A*, 74:13607, 2006.
- [75] Lei Wang, Xi Dai, Shu Chen, and X. C. Xie. Magnetism of cold fermionic atoms on the p band of an optical lattice. *Phys. Rev. A*, 78:023603, Aug 2008.
- [76] Lu Li, C Richter, J Mannhart, and RC Ashoori. Coexistence of magnetic order and two-dimensional superconductivity at $\text{LaAlO}_3/\text{SrTiO}_3$ interfaces. *Nat. Phys.*, 7(10):762–766, 2011.
- [77] Julie A Bert, Beena Kalisky, Christopher Bell, Minu Kim, Yasuyuki Hikita, Harold Y Hwang, and Kathryn A Moler. Direct imaging of the coexistence of ferromagnetism and superconductivity at the $\text{LaAlO}_3/\text{SrTiO}_3$ interface. *Nat. Phys.*, 7(10):767–771, 2011.
- [78] Karen Michaeli, Andrew C. Potter, and Patrick A. Lee. Superconducting and ferromagnetic phases in

- srtio₃/laalo₃ oxide interface structures: Possibility of finite momentum pairing. *Phys. Rev. Lett.*, 108:117003, Mar 2012.
- [79] S. Banerjee, O. Erten, and M. Randeria. Ferromagnetic exchange, spin-orbit coupling and spiral magnetism at the LaAlO₃/SrTiO₃ interface. *Nature Physics*, 9:626–630, October 2013.
- [80] C. Wu. Orbital frustration and ordering in p-band mott insulators. *Phys. Rev. Lett.*, 100:200406, 2008.